

## Analysing multitemporal SAR images

SHAUN QUEGAN<sup>1</sup>

THUY LE TOAN<sup>2</sup>

<sup>1</sup>Sheffield Centre for Earth Observation Science

University of Sheffield, Sheffield S3 7RH, UK

S.Quegan@sheffield.ac.uk

<sup>2</sup>Centre d'Etudes Spatiales de la Biosphère

18 avenue Belin, 31055 Toulouse, CEDEX France

thuy.letuan@cnes.cesbio.fr

**Abstract.** Applications of multitemporal SAR data in many cases require accurate estimates of the backscattering coefficient at each time. Here we describe how multitemporal and spatial filtering can be combined in a processing chain to greatly improve the radiometric accuracy of the data and how the general methods can be simplified in the case of ERS data. The results will be illustrated using ERS-2 images in the context of exploiting change detection for forest applications.

**Keywords:** Change detection, image filtering.

### 1 Introduction

A major advantage of satellite SAR is its ability to acquire precisely calibrated images which are unaffected by cloud. This means that time series of accurate measurements are available for environmental monitoring and applications. Measurements that can be used include the temporal change in the backscattering coefficient and, under special time interval and baseline conditions, interferometric coherence and phase difference. For operational applications, however, the preferred information is that from changes in the backscattering coefficient, since these are routinely available under almost all conditions for a satellite SAR. For mapping purposes, this requires making use of the differing temporal signatures of different land cover types. Important examples are found in forestry and agriculture. Forestry exploits the low temporal change of forests compared to other cover types (Grover et al., 1998; Le Toan et al., 1995). By contrast, rice mapping relies on the high temporal change associated with flooded rice (Le Toan et al., 1997). In more general agriculture, temporal signatures have been used to separate different crop types (for several examples, see Wooding et al., 1994).

However, exploiting such time series requires a processing chain which can first produce registered, calibrated images, then reduce the radiometric uncertainty in the measurements by temporal and spatial filtering and finally use the time sequence of backscattering coefficients to make decisions, for example about the type of land cover. Our main concern in this paper is the filtering step in the processing chain, whose purpose is to provide a best estimate of  $S^0$  at each pixel and at each time, given a multitemporal sequence of registered images. Multitemporal filtering is an example of a more general class of problems where several images of the same scene are available (for example, at different frequencies and polarisations) and we wish to combine them in some optimal way to recover the information they contain at each pixel. In Section 2, after displaying the general solution to this problem, we will describe how it becomes modified in

the case of ERS 35 day repeat PRI images from vegetated regions, to provide a particularly simple and effective algorithm.

The apparent simplicity of the algorithm is, however, complicated by the fact that it relies on local properties of the individual images in the multitemporal sequence. These must be estimated from the data, which introduces a spatial dimension into the algorithm and requires adaptive methods if spatial resolution is not to be severely degraded. These, and their effects on the statistics of the filtered image, are described in Section 3.

Filtering may be used to improve the visual appearance of an image, but it is often also used as a precursor to a decision step such as classification. In this case, the radiometric properties of the classes we wish to separate provide constraints on the accuracy with which the filters must estimate  $\mathbf{s}^0$ . In forest classification, the improvement in the estimates of  $\mathbf{s}^0$  provided by multitemporal filtering is often insufficient to meet the required accuracy. Accuracy is here thought of in terms of classification error, which in simple thresholding schemes is dependent on the overlap in the probability density functions (PDFs) of the different classes being considered. For the PDFs of interest here, this overlap depends on the differences between the backscattering coefficients of the target types we wish to discriminate and the width of the PDFs. A convenient measure of the width is given by the equivalent number of looks (ENL), which is defined by

$$\text{ENL} = \frac{\text{mean}^2}{\text{variance}} \quad (1)$$

In this expression, the statistical quantities are appropriate to an ideal uniform (untextured) target in which the only sources of fluctuation come from speckle, after whatever filtering operations have been applied to produce the final data. Increasing the ENL is equivalent to decreasing the width of the PDF. We assume that the ENL of the original data is known (for ERS PRI data, ENL = 3).

The ENL of the PRI data is inadequate for most classification purposes but can be greatly improved by multitemporal filtering, up to a limit imposed by the number of independent images available. Spatial filtering may then be necessary if successful classification relies on further increases in the ENL. There are many algorithms available to perform this task, but in Section 4 we will explain how the properties of ERS data from the 35 day repeat cycle suggest that a simple approach is most suitable when our interest is in vegetated targets. Section 5 provides a brief summary and our conclusions.

## 2 Multitemporal filtering

The problem of combining several images from the same scene in order to provide optimal reduction of speckle has been addressed by a number of authors (Oliver and Quegan, 1998; Bruniquel and Lopes, 1997; Novak et al., 1993). If only intensity data are available, as in our case, the general linear solution for producing a single image with minimal normalised variance is given in Oliver and Quegan (1998) as a weighted sum

$$J(x, y) = \sum_{i=1}^M A_i(x, y) I_i(x, y), \quad (2a)$$

where  $I_i$ ,  $i = 1, \dots, M$ , is the intensity value at position  $(x, y)$  in channel  $i$  out of  $M$  (registered) channels. The weighting coefficients are defined by the relation

$$\mathbf{A} \propto C_I^{-1} \mathbf{s} \quad (2b)$$

where  $\mathbf{A}^t = (A_1, \dots, A_M)$ ,  $\mathbf{s}^t = (\mathbf{s}_1, \dots, \mathbf{s}_M) = (\langle I_1 \rangle, \dots, \langle I_M \rangle)$  and  $C_I$  is the covariance matrix of the intensity data

$$C_I(i, j) = \langle I_i I_j \rangle - \langle I_i \rangle \langle I_j \rangle \quad (3)$$

In these expressions and subsequently we omit the positional coordinates  $(x, y)$ .

In this solution a single image is produced in which the speckle has been minimised, but in fact the image it produces is essentially featureless, unless there are strong variations in the local correlation structure. A more useful approach is to form  $M$  images of the form

$$J_k = \sum_{i=1}^M A_{ki} I_i \quad k = 1, \dots, M \quad (4a)$$

under the condition that  $J_k$  is unbiased, so that  $\langle J_k \rangle = \langle I_k \rangle$ , and  $J_k$  has minimum variance. This problem has the solution

$$A_k^t = \mathbf{s}_k \frac{C_I^{-1} \mathbf{s}}{\mathbf{s} \cdot C_I^{-1} \mathbf{s}} \quad (4b)$$

where  $A_k$  is the  $k$ th row of the coefficient matrix  $A$ . Notice that this simply normalises the core speckle-reduced image (equation (2)) and multiplies it by the local mean value of intensity in each of the  $M$  images. Hence it retains the optimising property of (2) while inputting structure into the  $M$  speckle-reduced images. The explicit scheme for calculating the  $A_k$  given by (4) also has an implicit form given in Bruniquel and Lopes (1997).

This treatment is designed for the general case where the set of images may be correlated, but becomes much simpler when correlation can be neglected. In this case,  $C_I$  reduces to a diagonal matrix in which

$$C_I(i, j) = \mathbf{s}_i^2 \mathbf{d}_{ij} \quad (5)$$

where  $\mathbf{d}_{ij}$  is the Kronecker delta, and the speckle reduction scheme becomes

$$J_i = \frac{\mathbf{s}_i}{M} \sum_{j=1}^M \frac{I_j}{\mathbf{s}_j} \quad i = 1, \dots, M. \quad (6)$$

Here the core speckle reducing filter (equivalent to (2)) is given by the summation; the scaling appropriate to each temporal image is provided by the  $\mathbf{s}_i$  outside the summation.

In principle, if the multitemporal filtering uses  $M$  uncorrelated  $L$ -look images, the operation described by (6) should provide filtered images with  $\text{ENL} = M \times L$ . Measured values on real images are reported in Section 3.2.

## 2.1 Comparison with ERS data

The expression given in (6) appears to be the most appropriate for ERS data from the 35 day repeat cycle over vegetated areas, since the residual correlation over this period is likely to be negligible. This is because, at C band, the primary scatterers are leaves, twigs and small branches. Over a month, this population of scatterers is unlikely to remain stable enough to maintain coherence. As a test of this, we show in Figure 1 the histogram of correlation coefficients for

registered ERS images of West Harling (an area of forest and farmland) on 5/5/92 and 22/9/92, using a window size of 5 x 5 pixels in calculating the correlation. Although the histogram is centred on 0, large values of the correlation coefficient occur. These values can be attributed to two factors. The first arises from sampling statistics. Calculations of the correlation coefficient between completely uncorrelated pairs of simulated images gave rise to fairly wide histograms, suggesting that much of the correlation indicated in Figure 1 is simply a sampling effect. The second is that in the ERS image there are objects, such as buildings, which would be expected to give high correlation. These make up a fairly small proportion of the scene, but contribute significantly to the tails of the histogram.

If we accept the arguments above, then it is not only inefficient to use the general expression (4) to filter the data, but this is in fact the wrong method to use, since it involves estimating a covariance matrix of intensity, with spurious non-zero values in the off-diagonal components associated with sampling. These non-zero values pass into the solution scheme and introduce error. For this reason, the simplified scheme given by (6) is more correct. It is also very easy to implement, involving no matrix operations, just weighting by the estimated mean local backscattering coefficients in the  $M$  images.

If we were using data from the Tandem missions, the full scheme described by (4) would be more appropriate, but the sampling problems described above would still occur. The only way around them appears to be to use sampling windows sufficiently large to reduce the tails of the sampling distribution.

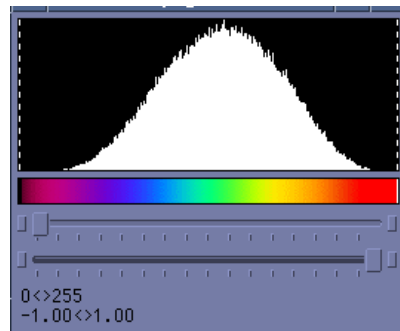


Figure 1 Correlation coefficients between ERS-1 images of West Harling on 5/5/92 and 22/9/92, estimated over a 5x5 window.

### 3 Spatial adaptivity

One of the potential advantages in using multitemporal filtering is that it appears to provide speckle reduction while preserving spatial resolution. However, it is important to observe that equation (6) requires local estimates of  $\mathcal{S}^p$  in each image. This involves using a window surrounding the pixel at the  $(x, y)$  position of interest, so that the multitemporal filtering includes spatial averaging. In order to prevent an associated loss of resolution, it is necessary to use an estimation scheme which is spatially adaptive. This is based on the approach in Lopes et al. (1993).

The filter adapts to local structure by first using the local coefficient of variation (CV) to test whether the region within the processing window is uniform and responding with various

geometric detectors if it is found not to be. Within the window, the CV is estimated by  $\hat{\mathbf{S}} / \hat{\mathbf{m}}$ , where the unbiased estimates of the the mean,  $\hat{\mathbf{m}}$ , and standard deviation,  $\hat{\mathbf{S}}$ , of the intensity are given by

$$\hat{\mathbf{m}} = \frac{1}{N} \sum_{i=1}^N I_i \quad (7)$$

and

$$\hat{\mathbf{S}} = \sqrt{\frac{\sum_{i=1}^N (I_i - \hat{\mathbf{m}})^2}{N-1}} \quad (8)$$

where  $I_{1...N}$  are the intensity values of the  $N$  pixels within the window. The theoretical distribution of the estimate  $\hat{\mathbf{S}} / \hat{\mathbf{m}}$  is unknown but found to be distributed around  $1/\sqrt{L}$ , where  $L$  is the number of looks in the image. By adding a small value,  $\mathbf{d}$  determined by a chosen confidence interval, to  $1/\sqrt{L}$ , the central pixel in the window is considered to belong to a homogeneous class if  $\hat{\mathbf{S}} / \hat{\mathbf{m}} \leq 1/\sqrt{L} + \mathbf{d}$  (note that this is one-sided), otherwise to a heterogeneous class. A filter which is trying to estimate the local value of  $\mathbf{s}^0$  can be made adaptive by the following algorithm (Lopes *et al*, 1993):

- (1) If  $\hat{\mathbf{S}} / \hat{\mathbf{m}} \leq 1/\sqrt{L} + \mathbf{d}$ , area is homogeneous, average over the whole window.
- (2) If  $\hat{\mathbf{S}} / \hat{\mathbf{m}} > 1/\sqrt{L} + \mathbf{d}$ , area is heterogeneous:
  - (2.1) Then apply structure (line and edge) detection.
  - (2.2) If no structure detected, apply point detection.
  - (2.3) If neither structure nor point is found, the area is textured.

Appropriate detectors are needed to perform the structure and point detections in steps (2.1) and (2.2). These are all developed from the ratio PDF for SAR images (Touzi *et al*, 1988).

### 3.1 The ratio PDF

Assume we have two uniform regions, containing  $N_1$  and  $N_2$  pixels respectively, whose true intensity ratio is  $R = \mathbf{s}_1 / \mathbf{s}_2$ , where  $\mathbf{s}_1$  and  $\mathbf{s}_2$  are the mean intensities of the two regions. If  $A_1, A_2, \dots, A_{N_1}$  and  $B_1, B_2, \dots, B_{N_2}$  are the two sets of pixel intensity values then the maximum likelihood estimate,  $\hat{r}$ , of  $R$  is given by the ratio of the average intensities:

$$\hat{r} = \frac{\bar{A}}{\bar{B}}. \quad (9)$$

Ratio detection should be independent of whether we choose  $\frac{\bar{A}}{\bar{B}}$  or  $\frac{\bar{B}}{\bar{A}}$  as the test ratio, so following (Touzi *et al*, 1988), we define a normalized ratio measure

$$\hat{r}_N = \min\left(\frac{\bar{A}}{\bar{B}}, \frac{\bar{B}}{\bar{A}}\right) \quad (10)$$

which can never exceed the value 1. The conditional PDF of  $\hat{r}$ , given  $R$ , is (Lopes *et al*, 1993)

$$p(\hat{r}_N | R) = \frac{1}{B(N_1 L, N_2 L) \cdot \hat{r}_N} \left( \frac{\left(\frac{N_2}{N_1}\right)^{N_2 L} \left(\hat{r}_N \frac{1}{R}\right)^{N_1 L}}{\left[\hat{r}_N \left(\frac{1}{R}\right) + \left(\frac{N_2}{N_1}\right)\right]^{(N_1 L + N_2 L)}} + \frac{\left(\frac{N_1}{N_2}\right)^{N_1 L} (\hat{r}_N R)^{N_2 L}}{\left[\hat{r}_N R + \left(\frac{N_1}{N_2}\right)\right]^{(N_1 L + N_2 L)}} \right) \quad (11)$$

where  $L$  is the number of looks, and  $B$  is the Beta function:

$$B(z, w) = \frac{\Gamma(z)\Gamma(w)}{\Gamma(z+w)}$$

Defining the contrast ratio of two homogeneous areas by  $C = \max[R, 1/R]$ , we note that  $p(\hat{r}_N | R) = p(\hat{r}_N | 1/R) = p(\hat{r}_N | C)$ .

The ratio PDF in (11) can be easily developed into PDFs of edge, line and point ratios by selecting the appropriate geometry in the processing window and modifying the values of  $N_1$  and  $N_2$  accordingly. The false alarm probability (the probability that  $r_N$  is less than some threshold when the two regions in fact have the same backscattering coefficient) can then be calculated for

each of these PDFs, and is given by  $\int_0^{r_T} p(r_N | 1) dr_N$ , where  $r_T$  is the detection threshold, since the

PDF for a uniform region simply sets  $C = 1$ .

The edge and line detectors are made independent of orientation by testing for edges and lines in several different directions. For a square window, horizontal, vertical and two diagonal orientations are used. The minimum values of the edge ratio,  $r_E$ , and the line ratio,  $r_L$ , calculated over all tested directions are used, as they provide the strongest evidence for an edge or line. These ratios are compared with the chosen thresholds for edge and line detections,  $r_{Emax}$  and  $r_{Lmax}$ . If  $r_E \leq r_{Emax}$ , an edge is detected, and if  $r_L \leq r_{Lmax}$ , a line is detected. The thresholds are all uniquely associated with the required false alarm using (10).

The intensity point ratio detector,  $r_p$ , uses the ratio of the average intensity in a point target region (a cross shape representing the point spread function of the imaging system) and the averaged intensity from the rest of the window. We then test whether the observed ratio of the average intensity of the point region and the pixels in the rest of the region is likely to have arisen purely from speckle, again using a threshold based on a fixed false alarm probability.

If, as a result of these tests, any feature or point is found, the filter estimates the mean intensity by averaging pixels only in the detected edge, line or point regions to which the central pixel belongs. This helps to preserve resolution and prevent blurring of features. Full details can be found in Lopes *et al.* (1993).

### 3.2 Examples of multitemporal adaptive filtering

In Figure 2 we illustrate the multitemporal filtering concepts introduced in Sections 2 and 3.1. Figure 2(a) shows a single ERS image from a sequence of 11 images available for the West Harling, UK, test site in 1997. Figure 2(b) is the 'featureless' result of the optimal speckle reducing operation resulting from equation (2), after combining all the images, but without correcting for the local intensity. The presence of features in the image indicates failures in the

spatial adaptivity when the filter window used for estimating the local intensity straddles an edge. Figure 2(c) shows the filtered image corresponding to Figure 2(a) after correction for the local intensity. Although a significant improvement on Figure 2(a), this image is still not very useful for feature detection. A marked further improvement in interpretability is provided when we combine images as multitemporal overlays, as in Figure 2(d), where the temporally filtered images for 23/5/97, 5/9/97 and 14/3/97 are overlaid as red, green and blue respectively. Here we have used the spatially adaptive estimates of local mean intensity.

An important issue for their subsequent use is the ENL of the filtered images. In principle, if the  $M$   $L$ -look images are uncorrelated, the operation described by (6) should provide filtered images with  $ENL = M \times L$ . Hence, the eleven 3-look ERS-2 images used to form Figure 2(b, c) should give rise to 33-look data after filtering. Measured values are of the order 22. This deviation from the ideal value can be explained by the errors in estimating the local intensity in (6); if this estimate is not accurate, the filter is no longer optimal and the ENL will decrease. Larger errors are likely when spatial adaptivity causes averaging over fewer pixels. Hence, the ENL is likely to vary spatially within the filtered image.

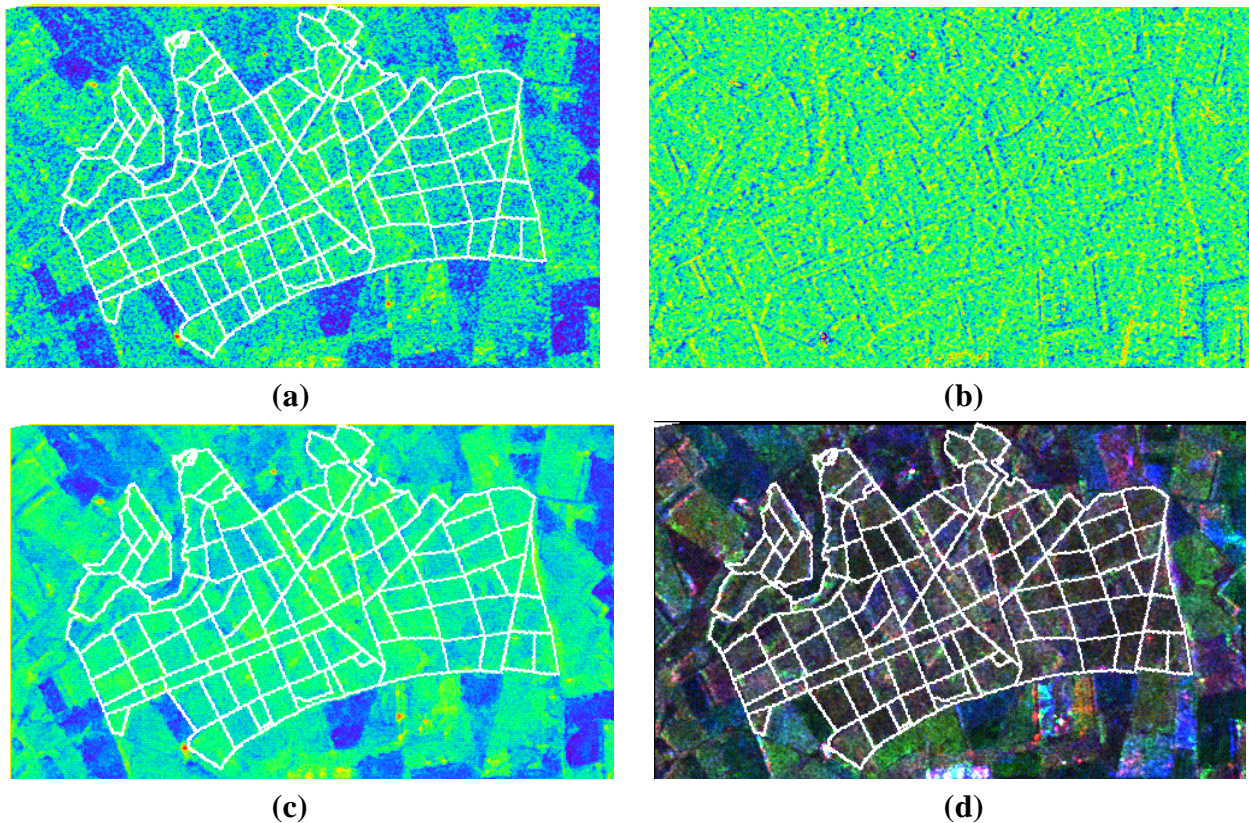


**Figure 2 (a) ERS-2 dB image of West Harling on 23/5/97**  
**(b) Featureless core (dB) image using 1997 ERS-2 data of West Harling**  
**(c) Temporal filtered image corresponding to 2(a)**  
**(d) Overlay of temporal filtered images**  
**(23/5/97 in red, 5/9/97 in green and 14/3/97 in blue)**

#### 4. Spatial filtering

For many purposes, the level of speckle filtering achievable by temporal filtering alone will be insufficient for the success of subsequent operations, such as classification. For example, probability of error is strongly dependent on ENL and acceptable false alarm rates often require large ENL (Oliver and Quegan, 1998; Rignot and van Zyl, 1997). In order to increase the ENL, spatial filtering is required after the temporal filtering. In the same way that consideration of the properties of the ERS 35 day repeat data led us to a particularly simple form of the multitemporal filter, we now use further arguments about these properties to derive the appropriate form of the spatial filter.

The essence of the spatial filtering approach lies in the formulation of the reconstruction problem; this is discussed at length in Oliver and Quegan (1998). For our purposes, we consider two approaches: local averaging (box filter) and local maximum a posteriori filtering with a gamma distributed prior (GMAP; Lopes et al., 1993).

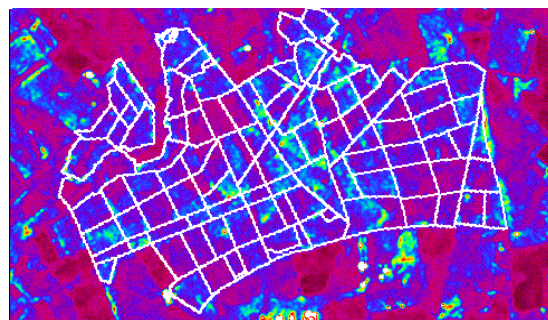
Local filtering makes assumptions about the statistical distribution of the backscattering coefficients of the population contained within the processing window. For averaging it is assumed uniform, while for GMAP it is assumed to be gamma distributed, so that the data are textured. In combination with speckle, these two models lead to the observed data being either gamma or K distributed, respectively. In addition, the GMAP filter makes use of the order parameter (ENL) of the speckle distribution and in its simple form assumes that this is the same everywhere. Finally, the GMAP filter is adversely affected by spatial correlation in the data, which affects its estimate of the underlying gamma distribution assumed for the backscattering coefficient.

Most of the assumptions of GMAP are violated at the spatial resolution and incidence angle of ERS PRI data. In most cases, there is little or no evidence for measurable texture in forest or agricultural areas, particularly at the scale of typical processing windows. (An important exception can occur in regions of medium scale topographic variation. Recent work has shown that for such regions in tropical forest, marked texture in the deforested areas provides good discrimination from the untouched forest. However, this is not the general situation.) Since GMAP is specifically designed for gamma distributed texture, this suggests it is not the appropriate filter to use. In addition, after temporal filtering, the data are spatially correlated (both because of point spread function effects in the original data and as a consequence of overlaps in the windows used to estimate local parameters at different pixels). Furthermore, sampling errors cause the number of looks to vary within the temporally filtered image, as discussed in Section 3.2.

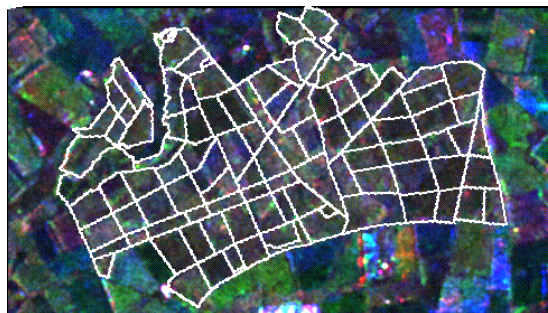
Both the latter effects also have an impact on the box filter. It is readily shown that for independent pixels each drawn from the same gamma distribution, the box filter provides the maximum likelihood estimate of  $\mathbf{s}^0$ . However, this is no longer true in the presence of either spatial correlation or variation in the ENL. The box filter nonetheless still provides a very simple unbiased estimate of  $\mathbf{s}^0$  under the assumption that its underlying distribution is uniform, rather than textured. There seems no reason from observations on the ERS PRI data to assume anything else in either forest regions or agricultural fields.

The discussion of spatial adaptivity in Section 3 was concerned with providing estimates of an image parameter using spatial averages in the presence of image structure. Although discussed in the context of temporal filtering, this is obviously equally applicable to spatial filtering and uses exactly the same methods. The only difference in the case of these two filters is in their response to the presence of texture; for GMAP the output will then be given by the filter developed by Lopes et al. (1993) while the box filter will treat this as a statistical fluctuation and average across the whole window.

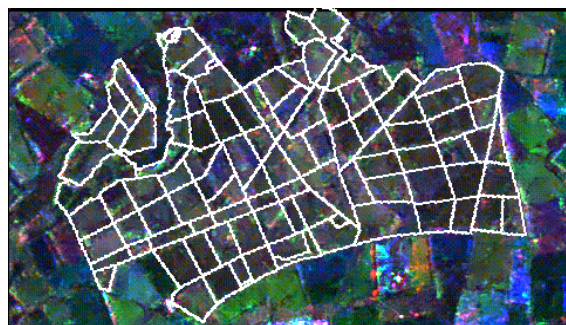
Figure 3(a) shows the effects of spatial filtering of the image shown as Figure 2(c) using the box filter, while Figure 3(b) and (c) show the overlay of the three spatially filtered images making up Figure 2(d), using the box and GMAP filters respectively.



(a)



(b)



(c)

Figure 3. (a) The image in Figure 2(c) spatially filtered by a 3x3 box filter  
(b) Overlay of the images in Figure 2(d) spatially filtered by a 3x3 box filter  
(c) As in (b), but using GMAP

It can be seen that the GMAP filter leads to images which appear sharper, probably because this filter does less averaging near edges. In effect, while box filtering can respond to edges only through the adaptivity of its processing window, GMAP gets a second chance through the statistical model it uses for the data. (This is a by-product, not a design feature of the filter, which as we have noted uses what is probably an inappropriate model for the ERS data.) The crisper aspect of the GMAP filtered data is related to the fact that it has done insufficient smoothing to produce good classification results in many circumstances, so that a further filtering step is required (Le Toan et al., 1995, 1997).

As with temporal filtering, the appropriate window size needs to be selected for use in either of these filters, but the problem is different. For the temporal filtering, the windows need to be big enough to allow accurate estimates of the local value of  $s^0$  in each image in the temporal sequence. In this case, the temporal filter will be close to its optimal performance and will yield an ENL near to its ideal value of  $ML$  (see Section 3). No further improvement in the ENL is possible using temporal filtering. For the spatial filter, bigger windows lead to continued improvements in ENL until the window size exceeds the scale length of the homogeneous land unit in the image (and assuming that the spatial adaptivity performs adequately). Hence the choice of window size is determined by the nature of the subsequent classification step and the ENL necessary to provide successful separation of the different classes.

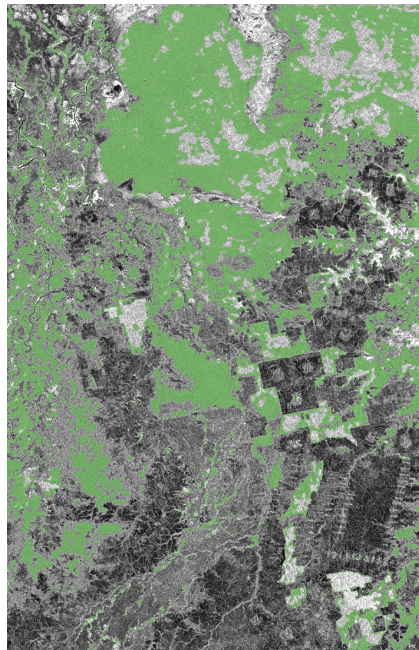


Figure 4. Forest/non-forest map of the Kuayagang area in Sumatra, derived from two ERS-1 images acquired on 1/12/93 and 5/8/94.

Note that the GMAP filter has been successfully used in several studies involving post filtering classification of ERS data (Le Toan et al., 1995, 1997). An example is shown in Figure 4, which is a forest/non-forest map of the Kuayagang area in Sumatra, derived from two ERS-1 images acquired on 1/12/93 and 5/8/94. Green is assigned to pixels with temporal change less than 1 dB, corresponding to forest, whereas the grey colour shows non-forest areas with higher temporal change between the wet and dry seasons. The different grey tones represent the backscatter intensity of the dry season data, used as an indicator of oil palm plantations (bright

grey), rubber plantations (medium grey) and bare or agricultural fields (dark grey). Here the discrimination based on change was aided by the large backscatter variation and the large dimension of the non-forest areas in the two images.

In this example, GMAP has been followed by a second spatial filtering step to remove excess variability in its output. Similar smoothing has been necessary in other applications of GMAP, either involving simple box averaging after filtering or post-classification cleaning. This suggests that the filtering step has not met its aim of providing a sufficiently accurate estimate of  $S^0$ . Indeed, the assumption of an underlying gamma distribution for the backscattering coefficient will lead to unacceptably high numbers of large pixel values in the output if it is incorrect. Attempts to use GMAP for tropical forest classification without subsequent operations on the filtered data did not prove successful, as the direct output from the filter was too noisy (Grover et al., 1998).

## 5 Conclusions

Multitemporal SAR data can be exploited to take advantage of information carried by changes in backscattering coefficient, which are relevant in many applications. Having multitemporal data available also allows us to improve the radiometric quality of the images by means of multitemporal filtering techniques. In the general case, the optimal speckle-reducing filter makes use of the correlation between images from different dates. However, for ERS data in the 35 day repeat cycle, the correlation between different dates over vegetated targets is normally very low. This leads to a particularly simple and easily implemented form of the temporal filter. Although in principle this preserves resolution, it requires local estimates of the backscattering coefficient, which both reduces the degree of filtering and leads to unwanted spatial blurring. In order to combat the latter, the estimates need to be made within locally adaptive windows. In many cases, the degree of smoothing afforded by temporal filtering alone is insufficient to support successful post-filtering operations such as classification, and spatial filtering is also necessary. The appropriate type of filtering depends on the correct model for the data of interest. The resolution and incidence angle of ERS mean that texture is only weakly present, if at all, at the scale of typical processing windows. This allows a rather simple approach to spatial filtering to be used, which again is much aided by being made adaptive.

## Acknowledgement

We would like to thank Jiong Jiong Yu of SCEOS and Florence Ribbes of CESBIO for much help, especially preparation of figures. We also thank the European Space Agency for the supply of ERS data.

## References

- Bruniquel, J. and Lopes, A., 1997, "Multi-variate optimal speckle reduction in SAR imagery", *Int. J. Remote Sensing* **18**, 603-627.
- Grover, K.D., Quegan, S and Yanasse, C.C.F., 1998, "Quantitative estimation of tropical forest cover by SAR", *I.E.E.E. Transactions on Geoscience and Remote Sensing* (in press).
- Le Toan, T., Hahn, T., Floury, N. Ribbes, F., Bruniquel, J. Lopes, A. and Wasrin, U.R., 1995, "Assessment of multitemporal ERS-1 data for deforestation monitoring in South Sumatra", TREES ERS-1 Study Final Workshop, JRC Ispra, February 1995.

- Le Toan *et al.*, 1997, "Rice crop mapping and monitoring using ERS-1 data based on experiment and modelling results", *I.E.E.E. Transactions on Geoscience and Remote Sensing*, **35**, 41-56.
- Lopes, A., Nezry, E., Touzi, R., and Laur, H., 1993, "Structure detection and statistical adaptive speckle filtering in SAR images", *Int. J. Remote Sensing*, **14**, No.9, 1735-1758.
- Novak, L.M., Burl, M.C. and Irving W.W., 1993, "Optimal polarimetric processing for enhanced target detection", *I.E.E.E. Trans. Aerospace Elect. Systems*, **29**, 293-305.
- Oliver, C.J. and Quegan, S., 1998, "Understanding synthetic aperture radar images", Artech House.
- Rignot, J.M. and van Zyl, J.J., 1993, "Change Detection Techniques for ERS-1 SAR Data", *I.E.E.E. Transactions on Geoscience and Remote Sensing*, **31**, No. 4, 896-906.
- Touzi, R., Lopes, A., and Bousquet, P., 1988, "A statistical and geometrical edge detector for SAR images", *I.E.E.E. Transactions on Geoscience and Remote Sensing*, **26**, 764-773.
- Wooding *et al.*, 1995, "Satellite radar in agriculture: Experience with ERS-1", ESA SP-1185.